Journal of Nuclear Materials 438 (2013) S346–S350

Contents lists available at SciVerse ScienceDirect

Journal of Nuclear Materials

journal homepage: www.elsevier.com/locate/jnucmat

Fast pedestal, SOL and divertor measurements from DIII-D to validate BOUT++ nonlinear ELM simulations

M.E. Fenstermacher [a,*,1], X.Q. Xu [a], I. Joseph [a], M.J. Lanctot [a], C.J. Lasnier [a], W.H. Meyer [a], B. Tobias [b], L. Zeng [c], A.W. Leonard [d], T.H. Osborne [d]

[a] Lawrence Livermore National Laboratory, Livermore, CA 94550, USA
[b] Princeton Plasma Physics Laboratory, Princeton, NJ 08543, USA
[c] University of California-Los Angeles, Los Angeles, CA 90095-7099, USA
[d] General Atomics, San Diego, CA 92186-5608, USA

ARTICLE INFO

Article history:
Available online 12 January 2013

ABSTRACT

This paper documents first work toward validation of BOUT++ nonlinear edge localized mode (ELM) simulations in X-point geometry, at experimental pedestal collisionality, against multiple diagnostic measurements of a well-characterized ELM event in DIII-D. The key to the BOUT++ simulations is the use of a hyper-resistivity model that effectively spreads the very thin current sheets that form in low collisionality nonlinear simulations, and allows for ELM driven magnetic reconnection at finite current density. Experimental ELM characterization includes multiple fast line-integrated diagnostic measurements revealing in–out divertor asymmetric response to ELMs, IRTV imaging at the divertor targets, visible emission in the divertor volume to test the extension of BOUT++ to X-point geometry, and forward modeling of new electron cyclotron emission imaging to test predictions of ELM filaments in the edge pedestal. Initial comparisons suggest optimized BOUT boundary conditions and model parameters, and show similarities between initial BOUT++ results and several measurements.

© 2013 Elsevier B.V. All rights reserved.

1. Introduction

The impulsive heat and particle losses due to unmitigated Type-I edge localized modes (ELMs) [1] are predicted to cause excessive erosion and damage to plasma facing components (PFCs) in future high power tokamak devices [2, and references therein]. Full nonlinear predictive capability for ELM energy loss, target heat flux deposition, etc. would be very valuable to predict PFC requirements for future reactor designs, and requirements for candidate ELM control techniques. Previously ELM simulations were limited to artificially high collisionality regimes due to numerical problems associated with very thin current sheets that form in low collisionality nonlinear simulations. A new hyper-resistivity model in the BOUT++ fluid MHD code [3] allows full nonlinear simulations at experimental collisionality, and therefore permits direct comparison of code predictions with multiple experimental measurements. The purpose of this paper is to document initial progress toward validation of this BOUT++ model, extended to X-point geometry, with fast ELM measurements on DIII-D.

The paper is organized as follows. The experimental characterization of ELM events in the DIII-D tokamak is given in Section 2. The results of linear and nonlinear BOUT++ simulations of this ELM are described in Section 3. A comparison of the initial simulation results with some of the experimental measurements is discussed in Section 4 leading to preliminary conclusions and plans for future validation work.

2. Experimental ELM characterization

The Type-I ELM characterized in this paper occurred in the standard ELMing H-mode phase of a discharge. Later in the discharge the plasma was subjected to significant $n = 2$ resonant magnetic perturbations (RMPs) that completely suppressed the Type-I ELMs [4]. The work reported here is the beginning of a continuing project to validate nonlinear BOUT++ simulations of both standard Type-I ELM dynamics and the effects of RMPs to achieve ELM suppression. The lower single-null (LSN) equilibrium plasma shape and evolution of basic plasma parameters for the DIII-D discharge are shown in Fig. 1. Steady-state conditions during the ELMing H-mode phase without the RMP were $I_p = 1.5$ MA, $B_T = 1.95$ T, average $P_{NBI} = 5.6$ MW, $R = 1.75$ m, $a = 0.6$ m, $\kappa = 1.82$, $\delta = 0.65$, $q_{95} = 3.64$, and $\beta_N = 2.0$. Regular Type-I ELMs at 40 Hz occurred from 2.0 to 2.4 s.

The crash and recovery of the ELM at 2241 ms (Fig. 2) were detected with multiple fast acquisition data chords in the pedestal,

* Corresponding author. Address: 13-466, c/o General Atomics, PO Box 85608, San Diego, CA 92186-5608, USA.
E-mail address: fenstermacher@fusion.gat.com (M.E. Fenstermacher).
[1] Presenting author.

0022-3115/$ - see front matter © 2013 Elsevier B.V. All rights reserved.
http://dx.doi.org/10.1016/j.jnucmat.2013.01.065

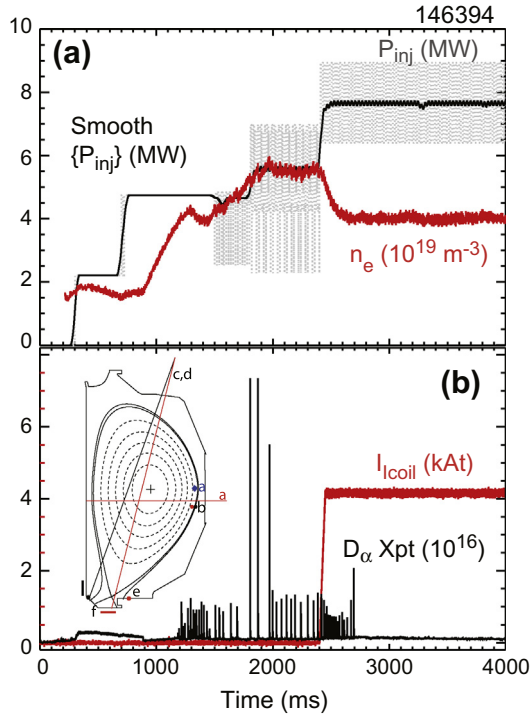

Fig. 1. Evolution of key parameters for DIII-D discharge 146,394 from which the ELM at 2241 ms was simulated with BOUT++, including (a) neutral beam power (MW) and line averaged density (10^{19} m^{-3}), and (b) I–coil current (kAt) and outer divertor D_α emission (au). Insert shows equilibrium shape and diagnostic locations for signals in Fig. 2(a–f).

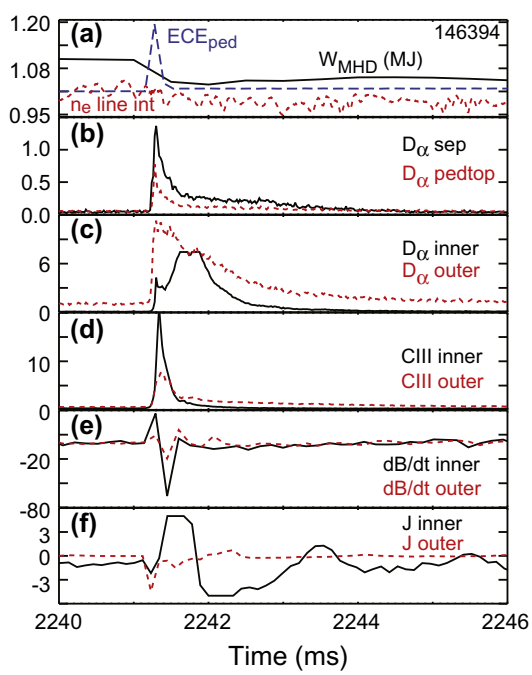

Fig. 2. Evolution of multiple local measurements during the Type-I ELM at 2241.15 ms including (a) total stored energy (MJ), line-integrated density along a horizontal midplane chord (1.4×10^{20} m^{-2}) and ECE emission near the top of the pedestal (au), (b) D_α emission from the top of the pedestal and near the separatrix at the LFS midplane (au), (c) D_α, and (d) CIII (465 nm) emission from the ISP and LFS X-point (au), (e) dB/dt (T/s), and (f) ion saturation current [j_{sat} (au)] from the ISP and OSP.

scrape-off layer (SOL) and divertor; this provides a significant database for validation of a BOUT++ nonlinear simulation of this instability event. Fig. 2a shows that this ELM produced a drop in the plasma stored energy of 6.5% (72 kJ from a 1.1 MJ plasma) and a reduction of the line integrated density of 5%. Fast transients were seen on an electron cyclotron emission (ECE) channel at the top of the pedestal, and on the outer midplane tangential D_α channels (Fig. 2b), which showed a larger transient in the SOL than at the pedestal top. Transients seen in the divertor included an immediate spike in the D_α chord viewing the low field side (LFS) X-point region, and a delayed, smaller response from the chord viewing the inner divertor leg (Fig. 2c). The response of CIII (465 nm) emission (Fig. 2d) was larger from the inner divertor chord than from the outer X-point measurement, as was the response of j_{sat} from a target mounted probe near the inner strike point (ISP) vs the outer strike point (OSP) (Fig. 2f). Also, the response on a magnetic probe below the floor near the ISP was larger than the corresponding response of a magnetic probe near the OSP (Fig. 2e). The combined responses in Fig. 2b–f are consistent with both ion sound speed parallel particle transport from an outer midplane ballooning instability (Fig. 2b, c, f) and effects of the burn-through of the detached inner leg by the ELM energy pulse (Fig. 2d and e). Finally, fast reflectometry profile measurements from the outer midplane (Fig. 3) showed the initial drop of pedestal density and broadening into the SOL, followed by rapid recovery of the SOL and gradual pedestal build-up. These measurements provide data to test multiple aspects of the ELM dynamics in the BOUT++ physics model.

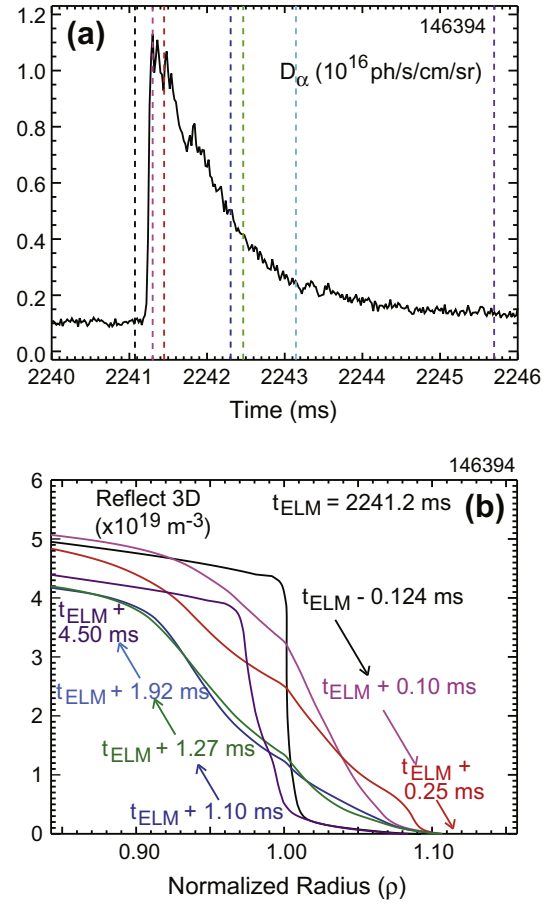

Fig. 3. Evolution of edge electron density profiles during the ELM with (a) temporal evolution from D_α emission in the outer divertor leg, and (b) multiple n_e profiles at times during the ELM evolution marked by vertical dashed lines in (a).

The effect of the ELM crash was also observed on several surface and volumetric diagnostics, including divertor IR emission showing broadening of heat deposition with multiple helical structures, and

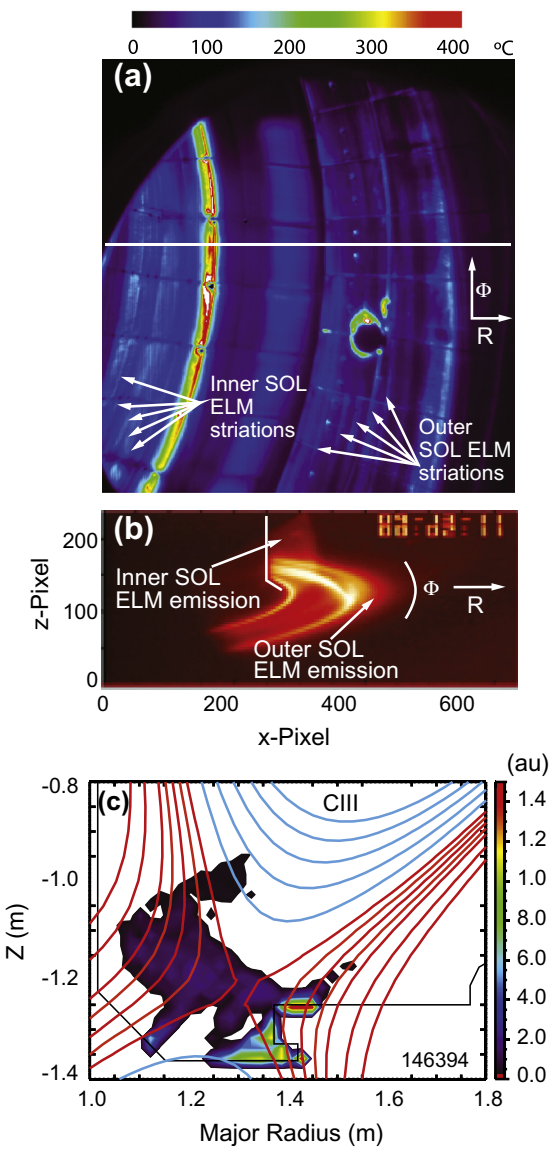

Fig. 4. ELM signatures on 2D diagnostics with (a) temperature change on the divertor target from IRTV data, (b) CIII (465 nm) volumetric emission profile during the ELM from tangentially viewing camera data and (c) 2D reconstructions of the CIII profile assuming toroidal symmetry.

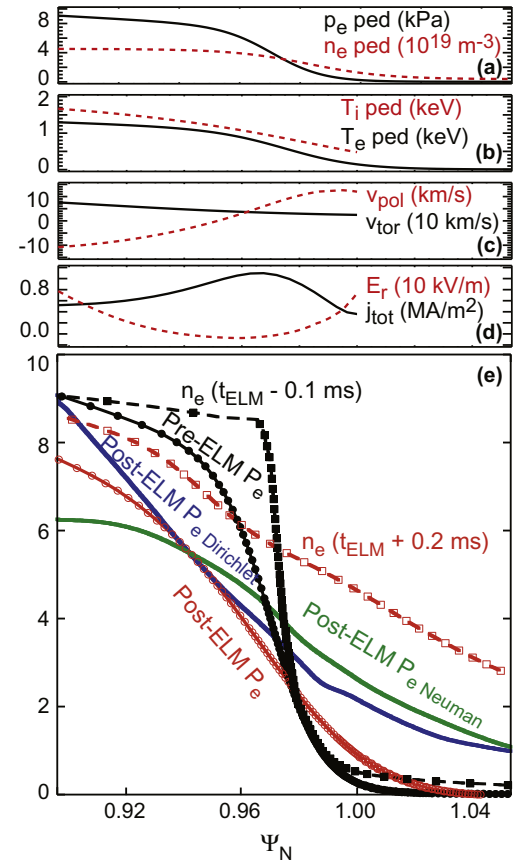

Fig. 5. Curve fits to pre-ELM radial profiles of plasma parameters in the pedestal from Thomson scattering and CER data including (a) electron pressure (kPa) and density (10^{19} m^{-3}), (b) electron and C^{6+} ion temperatures (keV), (c) toroidal (10 km/s) and poloidal (km/s) rotation and (d) radial electric field (E_r – kV/m) and edge current density including the bootstrap contribution (MA/m^2). In (e) a comparison of electron pressure profiles (Thomson scattering) pre(30–99%)-ELM (black solid) and post(0–10%)-ELM (red solid), electron density (reflectometer) at $t_{ELM} - 0.1$ ms (black dashed) and at $t_{ELM} + 0.2$ ms (red dashed) vs the BOUT++ simulated post-ELM pressure at $t_{ELM} + 0.11$ ms using a Dirichlet BC (blue) normalized to the pre-ELM data at $\Psi_N = 0.9$ and at $t_{ELM} + 0.06$ ms using a Neumann BC (green) with the same normalization. Reflectometer profiles shifted by −0.03 in Ψ_N (within radial accuracy) to align foot of pedestal with Thomson pressure profile. (For interpretation of the references to color in this figure legend, the reader is referred to the web version of this article.)

tangentially viewing visible emission showing broadening of the carbon emission in the divertor. In Fig. 4a the data from the IR camera show that the ELM event causes a substantial increase of the target temperature far into both the inner and the outer SOL regions, including multiple helical striations of the temperature as seen in other devices [5]. In Fig. 4b and c, CIII emission (465 nm) data show that the ELM broadens the visible emission profile substantially into the SOL at both the ISP and OSP.

3. BOUT++ linear and nonlinear ELM simulations

The ELM simulations in this paper were done with a three-perturbation-field (magnetic flux $\tilde{A}_{\|}$, electric potential $\tilde{\Phi}$, and pressure $\tilde{p}$) model [6,7] extracted from the complete BOUT++ two fluid MHD equations. Non-ideal effects (finite resistivity – $\nabla_{\perp}^2 A_{\|}$, diamagnetic drift, $E \times B$ drift, parallel viscosity, and thermal diffusivity) are retained and a hyper-resistivity or electron viscosity term ($\nabla_{\perp}^4 A_{\|}$) is added to facilitate ELM magnetic reconnection with finite current sheets at the low resistivity in experiments. The magnitude of the hyper-resistivity coefficient is set by the assumption that the anomalous electron viscosity is comparable to typical measured values of electron perpendicular thermal diffusivity [7]. In the simulations below, a constant Lundquist number $S = V_A R \mu_0/\eta = 10^8$ and a constant hyper-Lundquist number $S_H = V_A R^3 \mu_0/\eta_H = 10^{13}$ are used. This determines a constant value of resistivity $\eta/\mu_0 = 0.39\ \mathrm{m}^2/\mathrm{s}$ and hyper-resistivity $\eta_H/\mu_0 = 2.2 \times 10^{-5}\ \mathrm{m}^4/\mathrm{s}$ which corresponds to a constant anomalous kinematic electron viscosity $\mu_e = 7.6\ \mathrm{m}^2/\mathrm{s}$. Recent work [8] has shown that an increase of 10^3 in S_H only causes a factor of 2 increase in ELM size. The three-field equations are solved using a field-aligned (flux) coordinate system with shifted radial derivatives [7] on a periodic domain in the parallel coordinate (with a twist-shift BC) and in toroidal angle.

The BOUT++ ELM simulations were run with as many of the input parameters as possible taken from experimental measurements. The kinetic plasma profiles needed for the calculation were obtained by averaging data from the last 70% of the ELM cycle (i.e., 30–99%) for the ELM at 2241 ms. Fig. 5a–d shows the fitted profiles of n_e, T_e, p_e from Thomson scattering measurements, T_i,

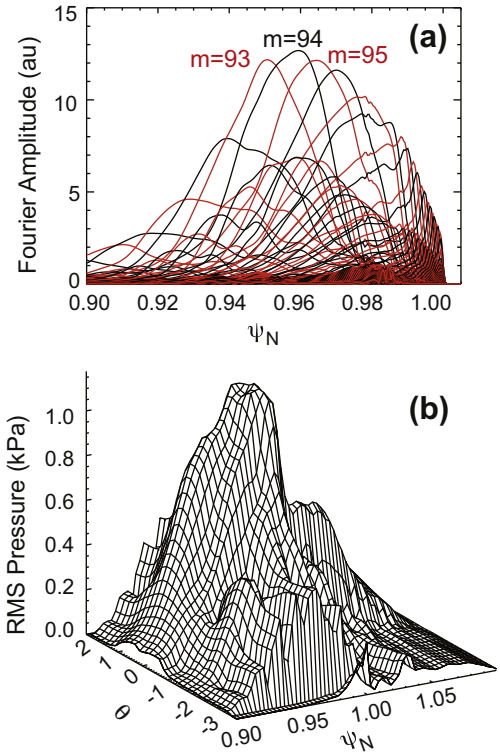

Fig. 6. BOUT++ linear simulation results using a Neumann BC including (a) radial structure of poloidal harmonics (alternating red and black curves as m -number increments by 1) for $n = 24$ linear instability mode ($m = nq = 94$ for black curve peaking at $\Psi_N = 0.96$), and (b) 2D structure of the RMS pressure perturbation during the initial nonlinear ELM crash at $t_{ELM} + 70$ μs (poloidal angle in radians referenced to outer midplane). (For interpretation of the references to color in this figure legend, the reader is referred to the web version of this article.)

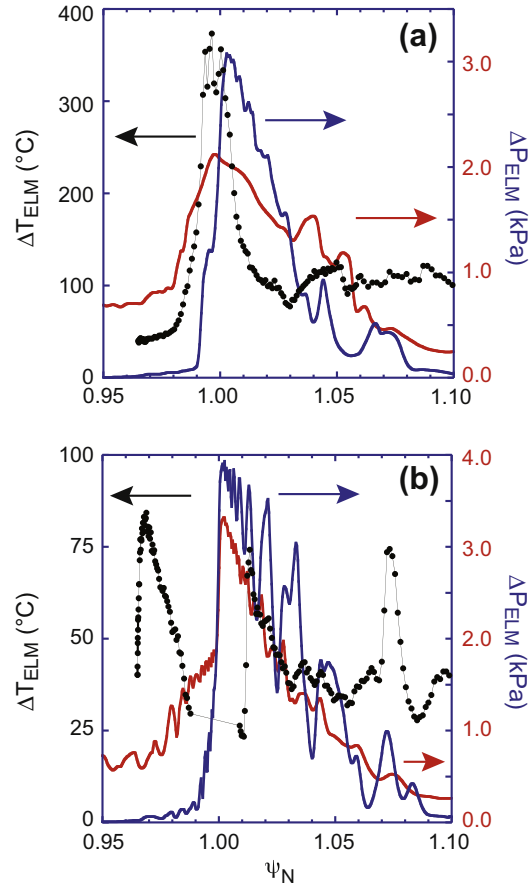

Fig. 7. Divertor target surface temperature perturbation [black — (°C)] [radial cut of Fig. 4a IRTV data at horizontal white line] and BOUT++ target pressure perturbation profiles [red — Dirichlet BC, blue — Neumann BC (kPa)] vs normalized poloidal flux (Ψ_N) for the (a) inner and (b) outer SOL regions. Note that in (b) the outer divertor IRTV view for $0.985 < \Psi_N < 1.01$ is occluded by the outer baffle shelf. (For interpretation of the references to color in this figure legend, the reader is referred to the web version of this article.)

toroidal rotation, poloidal rotation and radial electric field (E_r) from charge exchange recombination (CER) data, and the edge current profile including the bootstrap contribution calculated from the data fits using the Sauter formula [9]. The electron and ion pedestal collisionalities [9] were $\nu_e^* = 0.4$ and $\nu_i^* = 0.18$ respectively. These profiles, plus core current profile data from motional Stark effect (MSE) measurements, were used to generate the kinetic EFIT equilibrium that provided the flux surface geometry for the simulations. For these initial simulations, the E_r within BOUT++ is assumed to balance the ion pressure gradient, so that there are no net equilibrium ion flows.

BOUT++ linear simulations indicated that the plasma with the profiles shown in Fig. 5 was unstable to peeling–ballooning modes. This is consistent with independent linear stability calculations from the ELITE code [10]. The BOUT++ linear simulations show that the growth rate peaks for toroidal modes between $n = 15$ and $n = 25$, with a radial mode structure that displays both broad ballooning and narrow peeling features. Fig. 6a shows the radial structure of the poloidal harmonics of the pressure perturbation during the initial linear phase when the toroidal mode number is $n = 24$. A parallel viscosity in the range 3.9–7.8 $\times 10^6$ m^2/s was necessary to obtain convergence of the peeling mode structure near the X-point; the peeling mode components are stronger at lower viscosity.

The initial BOUT++ nonlinear simulations show rapid saturation of the RMS ELM pressure perturbation in about 6 μs at $t \sim 60$ μs, and propagation of the ELM structure into the SOL near the outer midplane (Fig. 6b) during the ELM crash that starts at $t = 70$ μs. Nonlinear simulations have been done with both Dirichlet (fixed pressure) and Neumann (fixed pressure gradient — Fig. 6) boundary conditions (BCs) on the inner edge of the computational grid, using a parallel viscosity of 1.2×10^7 m^2/s and a parallel thermal diffusivity of 3.9×10^7 m^2/s. A comparison of the pedestal electron pressure profile (Thomson scattering – black and red solid), density profile (reflectometer – black and red dashed) and the BOUT++ solutions (blue and green) before and after the ELM event (Fig. 5e) shows that the Dirichlet solution underestimates the SOL perturbation and the Neumann solution overestimates the perturbation at the top of the pedestal. The fractional drop of the pressure at the location of the pre-ELM pedestal top in the Dirichlet solution at 0.11 ms (30%) is similar to the drop of the density from the reflectometer at 0.20 ms (25%), but larger than the pedestal density drop at 0.10 ms (18%). Fig. 7 shows a comparison of the spatial structure of the BOUT++ ELM pressure perturbation at the divertor target using either the Dirichlet or Neumann BCs, with the spatial structure of the surface temperature perturbation measured by IRTV. Both the separation and magnitude of SOL striations ($1.02 < \Psi_N < 1.08$) on the outer target (Fig. 7b) are more similar to the IR data for the Dirichlet BC case. For the inner divertor SOL striations, Fig. 7a shows narrower separation in both BOUT++ simulations than in the IR data, although the width of the strike-point peak ($0.99 < \Psi_N < 1.02$) is more similar for the case with Neumann BC. Future simulations with a 6-perturbation-field model (separate n_e, T_e and T_i perturbations) and a fixed energy flux inner grid BC

should allow direct comparison of calculated and measured target heat flux and CIII visible emission.

4. Summary and outlook

The DIII-D fast diagnostic set provides multiple measurements of the evolution of the pedestal, SOL and divertor plasmas during an ELM cycle for validation of BOUT++ linear and nonlinear ELM simulations. Initial results from simulations run to several 100 μs with Dirichlet and Neumann BCs show similarities to measurements of the normalized outer midplane pedestal top pressure and density perturbations, and to the separation of perturbation striations at the outer divertor target. They also suggest that it will be necessary to incorporate a fixed flux BC, grids with inner boundary much further in (vis. $\Psi_N \sim 0.5$) and simulations run for much longer (several ms) to better match the measured ELM energy loss, midplane pedestal pressure profile perturbation and target heat flux striations. Future simulations will also include comparison of predicted ELM emission structure with data from ECEI in the pedestal [11] and images (both IR and line filtered visible emission) from a new tangentially viewing periscope installed on DIII-D. Past experiments in DIII-D with a limited poloidal view of the edge [12] showed that ELM CIII emission from the SOL can compare well with calculated linear ELM structure from ELITE. The wide-angle poloidal view of CIII emission from the new periscope will provide another strong test of BOUT++ linear and nonlinear predictions of the ELM structure.

Acknowledgments

This work was supported in part by the US Department of Energy under DE-AC52-07NA27344, DE-AC02-09CH11466, DE-FG02-08ER54984, and DE-FC02-04ER54698. M.E.F. would like to gratefully acknowledge B.I. Cohen for his effort coordinating the BOUT++ aspects of this project.

References

[1] H. Zohm, Plasma Phys. Control. Fusion 38 (1996) 105.
[2] A. Loarte et al., Proc. 23rd IAEA fusion energy conference, Daejeon, Korea (2010).
[3] B. Dudson, Comput. Phys. Commun. 180 (2009) 1467.
[4] M.J. Lanctot et al., Complete suppression of large Type-I edge localized modes using multi-harmonic magnetic perturbations in DIII-D, Nucl. Fusion. submitted for publication.
[5] T. Eich et al., J. Nucl. Mater. 337 (2005) 669.
[6] X.Q. Xu et al., Phys. Rev. Lett. 105 (2010) 175005.
[7] X.Q. Xu et al., Nucl. Fusion 51 (2011) 103040.
[8] X.Q. Xu, P.W. Xi, A.M. Dimits, Theory and gyro-fluid simulations of edge-localized-modes, Proc. 24th IAEA fusion energy conference, San Diego, California, 2012, Paper TH/5-2Rb.
[9] O. Sauter, C. Angioni, Y.R. Lin-Liu, Phys. Plasmas 6 (1999) 2834.
[10] P.B. Snyder, H.R. Wilson, X.Q. Xu, Phys. Plasmas 12 (2005) 056115.
[11] B.J. Tobias et al., Rev. Sci. Instrum. 83 (2012) 10E329.
[12] M.E. Fenstermacher et al., Nucl. Fusion 45 (2005) 1493.